ACS APPLIED ENERGY MATERIALS

Forum Article

Cite This: ACS Appl. Energy Mater. 2019, 2, 37−46

www.acsaem.org

Photocatalytic Reduction of CO_2 to CO and Formate: Do Reaction Conditions or Ruthenium Catalysts Control Product Selectivity?

Roberta R. Rodrigues,[†] Chance M. Boudreaux,[‡] Elizabeth T. Papish,*[,‡] and Jared H. Delcamp*[,†]

[†]Department of Chemistry and Biochemistry, University of Mississippi, Coulter Hall, University, Mississippi 38677, United States

[‡]Department of Chemistry and Biochemistry, University of Alabama, Shelby Hall, Tuscaloosa, Alabama 35487, United States

Supporting Information

ABSTRACT: The photocatalytic reduction of CO_2 can generate a number of products with CO and HCO_2^- being two of the most commonly observed. Frequently, the selective formation of one of these products is presumed to be the result of catalyst design. However, several common variables are present when exploring the photocatalytic CO_2 reduction reaction. In order to better understand the origin of selectivity in this reaction, the choices of solvent, electron and proton source, photosensitizer (PS), and catalyst were evaluated in photocatalytic CO_2 reduction reactions. Intriguingly, highly selective catalysts for CO or HCO_2^- under one set of conditions can be transformed by these environmental choices into becoming highly selective for the opposite product while retaining high turnover numbers. This highlights the importance of carefully considering reaction conditions before ascribing catalyst selectivity to an inherent molecular design property.

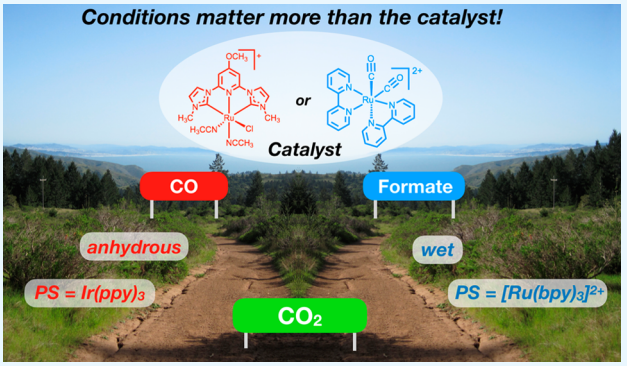

KEYWORDS: *photocatalytic CO_2 reduction, homogeneous, ruthenium catalysts, NHC pincer, photosensitized*

1. INTRODUCTION

Solar-to-fuel conversion is an attractive way to produce renewable, clean fuels from abundant CO_2.[1−4] A number of products may be formed during the catalytic reduction of CO_2.[5−7] An understanding of photocatalytic reactions that can drive and control product distributions with visible light is critically needed to enable the rational design of practical solar-to-fuel systems. Ideally, solar energy could be used to power a water oxidation catalyst coupled with a carbon dioxide reduction catalyst for a sustainable fuel generating energy conversion process. Controlling the product selectivity for the CO_2 reduction reaction to give a single product is desirable. Thus, studies focusing on this half-reaction by employing sacrificial electron donors (SEDs) to simplify catalytic systems are warranted in order to more rapidly identify highly selective, efficient CO_2 reduction systems.

Most commonly, homogeneous catalysts in photocatalytic CO_2 reductions produce CO or HCO_2^- as the primary products.[8,9] Often selectivity for these products is rationalized as catalyst controlled with research focusing on catalyst design as a primary method of product selectivity control. However, a myriad of conditions are commonly used in homogeneous photocatalytic CO_2 reduction reactions including selection of (1) a CO_2 solubilizing solvent such as *N*,*N*-dimethylformamide (DMF) or acetonitrile (MeCN), (2) electron and proton sources such as 1,3-dimethyl-2-phenyl-2,3-dihydro-1*H*-benzoimidazole (BIH), triethylamine (TEA), 1-benzyl-1,4-dihydronicotinamide (BNAH), or water, (3) a photosensitizer (PS) such as $Ir^{III}(ppy)_3$ or $[Ru^{II}(bpy)_3]^{2+}$ (where ppy is 2-phenylpyridine and bpy is 2,2′-bipyridine), and (4) a number of catalyst designs. Understanding which catalysts from the literature are selective for CO versus HCO_2^- formation becomes challenging if any of these components induce a significant CO_2 reduction product selectivity.

In order to use literature reports to rationally design next generation catalyst systems that are highly selective, an understanding of how each component affects selectivity is needed. To probe the influence of each component, two ruthenium precatalysts were selected from the literature which are reported to be selective for formate in the case of $[Ru^{II}(bpy)_2(CO)_2]^{2+}$ and selective for CO in the case of $[Ru^{II}(C^{Me}N^{OMe}C^{Me})(MeCN)_2Cl]^+$ (referred to as $[Ru^{II}(CNC)Cl]^+$ below) under the photocatalytic reaction conditions analyzed (Figure 1).[8,10,11] For each catalyst, the solvent, photosensitizer, and proton and electron sources were varied systematically to elucidate the effect of each component on CO versus HCO_2^- selectivity.

Special Issue: New Chemistry to Advance the Quest for Sustainable Solar Fuels

Received: September 14, 2018
Accepted: October 31, 2018
Published: November 13, 2018

DOI: 10.1021/acsaem.8b01560
ACS Appl. Energy Mater. 2019, 2, 37−46

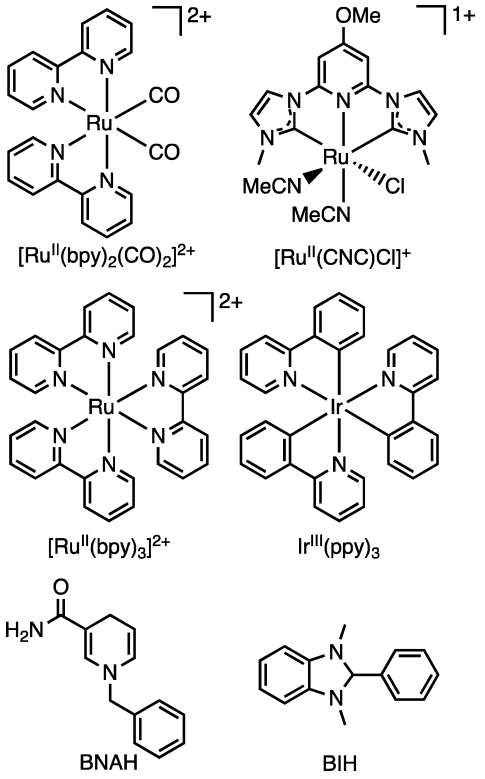

Figure 1. Catalysts (top), PSs (middle), and SEDs (bottom) used in these studies.

2. EXPERIMENTAL SECTION

2.1. Photocatalysis General Information. A neutral white light LED (Thorlabs, MNWHL4; color temperature, 4900 K) mounted with a collimation adaptor (Thorlabs, SM2F32-A; lens, Thorlabs, ACL50832U-A, with antireflective coating range 350−700 nm) was used as the light source for the photocatalytic experiments. The photocatalytic reaction vessel was set at a distance equaling 1 sun intensity across the white light emission range (380−750 nm), which was determined by using a power meter and a xenon lamp solar simulator measured at 1 sun intensity prior to placing a band-pass filter (from 380 to 750 nm) and measuring the power output. The reaction vessel was then placed at a distance from the LED to which the solar simulator power output through the band-pass filter matched. Calibration experiments were performed with $[Ru^{II}(bpy)_2(CO)_2]^{2+}$, $[Ru^{II}(bpy)_3]^{2+}$, BIH, TEA, and DMF to show results within ±2% turnover number (TON) values for the LED system when compared to unfiltered solar simulator measurements. Head space analysis was performed using a gastight syringe with stopcock and an Agilent 7890B gas chromatograph equipped with an Agilent PorapakQ 6 ft, 1/8 O.D. column. Quantitations of CO and CH_4 were made using an FID detector with the gases passing through a methanizer, while H_2 was quantified using a TCD detector (see Supporting Information Table S1 for H_2 production values). All reported values are the average of two experiments typically within ±5%. The lines added to the TON versus time plots are only to aid the eye in tracking data points and are not intended to imply any additional information. All calibrations were done using standards purchased from BuyCalGas.com. For all experiments involving *N*,*N*-dimethylformamide, DMF was freshly distilled by discarding the first 20% of the initial volume during vacuum distillation, and then changing flasks to a flame-dried round-bottom flask for the next 60% of the original volume (500 mL typically) which was used in the photoreactions. The solvent was stored out of light, in the freezer under N_2, and used within 2−3 weeks. All experiments with DMF were also run under N_2. All background reactions were minimal and were subtracted from the values obtained under CO_2. Acetonitrile (MeCN) was freshly distilled prior to use.

2.2. Example Photocatalysis Procedure. BIH (0.05 g, 0.2 mmol), MeCN (6.0 mL), and catalyst (0.2 mL from a 1×10^{-3} M MeCN solution) were added to a 17 mL Pyrex test tube. The solution was bubbled vigorously with CO_2 for at least 15 min until the solution volume reached 1.9 mL, and then 0.1 mL of degassed TEA was added to the mixture. For reactions involving water, 0.2 mL of H_2O was added to the reaction mixture prior to the reaction mixture being degassed with CO_2. The reaction vessel was sealed with a rubber septum and irradiated with a neutral white collimated LED.

2.3. Cyclic Voltammetry Procedure and Instrumentation. A CH Instruments electrochemical analyzer (CHI-600E) was used to conduct cyclic voltammetry (CV) measurements in the presence of Ag/AgCl as the reference electrode, platinum as the counter electrode, and glassy carbon as the working electrode with 0.1 M *n*-Bu_4NPF_6 as the supporting electrolyte. CVs were done in MeCN and DMF as solvent and referenced against ferrocenium/ferrocene (Fc^+/Fc). For each experiment the concentration of catalyst was kept constant at 1 mM. Before each measurement, the solution was degassed with Ar or CO_2 (for ∼15 min). To avoid concentration changes for the electrolyte and catalyst during degassing, the CV experiment was set up at the desired concentration, the solvent level marked, and then pure acetonitrile (2 mL) added. The mixture was then degassed with Ar or CO_2 until the solvent evaporated to the original marked volume.

2.4. UV−Vis Procedure and Instrumentation. UV−vis spectra were measured with a Cary 5000 instrument. UV−vis spectra of

Table 1. Catalyst, PS, and Electron Source Electrochemical and Photophysical Properties

chemical	solvent	λ_{max}^{abs} (nm)	λ_{onset}^{abs} (nm)[a]	λ_{max}^{emis} (nm)	$E_{(S/S^-)}$ (V, N_2)[b]	$E_{(S/S^-)}$ (V, CO_2)[b]	$E_{(S^*/S^-)}$ (V)[b]	$E_{(S+/S)}$ (V)[b]
$[Ru^{II}(bpy)_2(CO)_2]^{2+}$	MeCN	320	350		−1.32,[c] −2.42[c,d]	−1.90[c]		
$[Ru^{II}(bpy)_2(CO)_2]^{2+}$	DMF	330	380		−1.35,[c] −2.52[c,d]	−1.95[c]		
$[Ru^{II}(CNC)Cl]^{+}$	MeCN	403	480		−2.30[c]	−2.20[c]		
$[Ru^{II}(CNC)Cl]^{+}$	DMF	450	530		−2.35[c]	−2.20[c]		
$[Ru^{II}(bpy)_3]^{2+}$	MeCN	451	550	601	−1.72	−1.73	0.53	
$[Ru^{II}(bpy)_3]^{2+}$	DMF	454	550	607	−1.71	−1.72	0.54	
$Ir^{III}(ppy)_3$	MeCN	485	500	541	−2.61	−2.61[c]	0.06	
$Ir^{III}(ppy)_3$	DMF	488	505	536	−2.64	−2.55[c]	−0.03	
BIH	MeCN							−0.10[c]
BIH	DMF							−0.24[c]
BNAH	DMF							0.00[c]
TEA	MeCN							0.42[c]
TEA	DMF							0.22[c]

[a]Onset values are measured from the intercept of a tangent line with the *x*-axis on the lower energy side of the curve (see SI). [b]Values are versus ferrocenium/ferrocene. [c]Irreversible wave onset (see SI). [d]Second reduction potential.

DOI: 10.1021/acsaem.8b01560
ACS Appl. Energy Mater. 2019, 2, 37−46

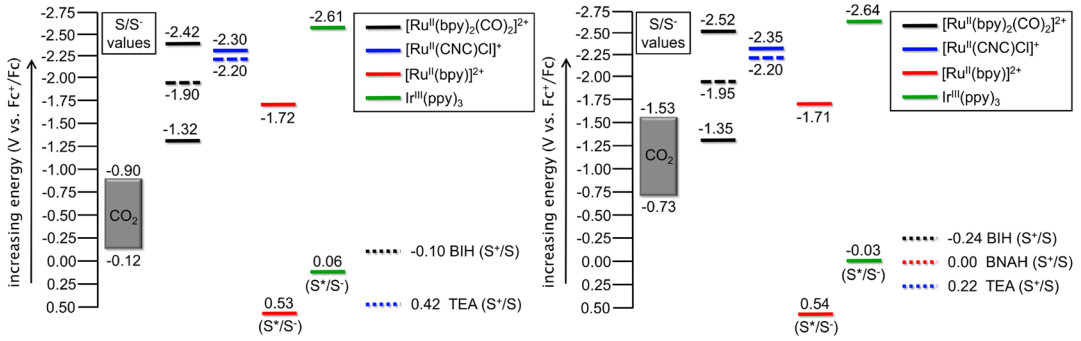

Figure 2. Energy level diagrams based on cyclic voltammetry and optical properties of the catalysts, PSs, and SEDs in MeCN (left) and DMF (right). The range for the standard reduction potential of CO_2 is dependent on pK_a with the lower energy value taken as the standard potential at pK_a ~ 0 and the upper limit defined by the estimated pK_a of carbonate (~13) in MeCN and DMF.[19−21] Solid lines are ground state and excited state reduction potentials under argon, long dashed lines are reduction potentials under CO_2, and short dashed lines are oxidation potentials.

$[Ru^{II}(bpy)_2(CO)_2]^{2+}$, $[Ru^{II}(CNC)Cl]^{+}$, $[Ru^{II}(bpy)_3]^{2+}$, and $Ir^{III}(ppy)_3$ were taken in MeCN and DMF.

2.5. Emission Curve Procedure and Instrumentation. Emission spectra were taken on a PerkinElmer LS55 fluorescence spectrometer. Emission spectra of $[Ru^{II}(bpy)_3]^{2+}$ and $Ir^{III}(ppy)_3$ were taken in MeCN and DMF at 1 mM concentrations after solvents were degassed with N_2 for 20 min prior to measurements. A photoexcitation wavelength of 455 nm was used for $[Ru^{II}(bpy)_3]^{2+}$, and a photoexcitation wavelength of 495 nm was used for $Ir^{III}(ppy)_3$. The sealed cuvette containing the samples was then degassed further with a balloon of N_2 for approximately 2 min, and the spectra were then taken.

2.6. ^{1}H NMR Formate Detection. This procedure is a modified approach from that used in the literature.[10,12] Upon reaction completion, 0.8 mL of the reaction solution was taken into a syringe and added to a 4 mL vial. The vial was left open for several minutes to allow CO_2 to escape in order to prevent DBU (1,8-diazabicyclo[5.4.0]undec-7-ene) from forming a DBU−CO_2 adduct.[13] To this solution was added 36 μL of DBU. The mixture was then sonicated for 10 min at room temperature. Next, 1.16 mL of a 1.19 mM ferrocene solution (in MeCN-d_3) was added to the mixture. The vial was thoroughly mixed, and then an NMR spectrum was taken on a 500 or 300 MHz NMR spectrophotometer with an extended D1 delay of 10 s and a minimum of 200 scans. The ratio of the formate peak (~8.7 ppm) and the ferrocene peak (~4.2 ppm) was then compared to a calibration curve as previously reported.[10] All NMR spectra were evaluated with MestReNova software to ensure level baselines in the analyte region prior to integrating peaks. Formate analysis using this technique requires stopping the reaction. Reactions were deemed complete once CO production halted since CO production can be monitored in real time.

3. RESULTS AND DISCUSSION

3.1. Thermodynamic Considerations. In addition to selecting these precatalysts for this study based on their reported different product selectivities, each of these catalysts should be amenable to varying the reaction components while maintaining thermodynamically viable electron transfer events (Table 1, Figure 2). In each case the thermodynamics of the precatalyst were analyzed via CV and UV−vis absorption spectroscopy in both solvents used in this study, MeCN and DMF (Figures S1−S6). The energetics of catalytic intermediates can be challenging to probe; however, the suitability of each precatalyst to generate an active catalyst can readily be evaluated via CV measurements. $[Ru^{II}(bpy)_2(CO)_2]^{2+}$ was found to generate a catalytic current under CO_2 atmosphere which is not observed when compared with argon in both MeCN and DMF at approximately −1.90 V versus Fc^+/Fc (Figure S1, Table 1).[10] The first reduction potential remains the same under argon and CO_2, and the catalytic current enhancement occurs at a potential between the first and second reduction potential observed under argon indicating that CO_2 likely binds to the Ru complex after the first reduction. $[Ru^{II}(CNC)Cl]^{+}$ shows a catalytic current enhancement at the first reduction potential under CO_2 when compared with argon at the same potential for both MeCN and DMF (Figure S2). Since the reduction potential is the same under both atmospheres, an electron is likely added first prior to catalytic activity. This catalytic activity occurs at −2.20 V versus Fc^+/Fc in both MeCN and DMF, which is about 300 mV more negative than that observed for $[Ru^{II}(bpy)_2(CO)_2]^{2+}$ (Table 1). The reduction potential of $[Ru^{II}(bpy)_3]^{2+}$ in both DMF and MeCN occurs near −1.72 V versus Fc^+/Fc (Table 1, Figure S3). Given that the electron transfer event from $[Ru^{II}(bpy)_3]^{1+}$ to either precatalyst is uphill in energy,[14] the active catalyst is expected to be accessed more slowly than if a downhill electron transfer from a reduced photosensitizer were compared if both reduced states were generated in similar concentrations (Figure 2). Comparatively, $Ir^{III}(ppy)_3$ is significantly harder to reduce and gives a strongly reducing anion at approximately −2.63 V versus Fc^+/Fc in both MeCN and DMF (Table 1, Figure S4). Since the electron transfer from $[Ir^{III}(ppy)_3]^{-}$ is significantly downhill to both precatalysts,[15] a more rapid generation of active catalyst is possible although the concentration of reduced photosensitizer in solution must also be considered. Additionally, the stronger reducing ability of $[Ir^{III}(ppy)_3]^{-}$ versus $[Ru^{II}(bpy)_3]^{+}$ could allow for both (1) access to reduced catalytic intermediates that are inaccessible otherwise and (2) more facile electron transfer events within a photocatalytic cycle if Marcus theory kinetics are applied.[16−18]

To evaluate the thermodynamics for the generation of the reduced photosensitizers, emission spectrum of the photosensitizers was taken in both MeCN and DMF (Figures S7 and S8). The excited state reduction potential was estimated from the equation $E_{(S^*/S^-)} = E_{(S/S^-)} + E_g^{\text{opt emis}}$, where $E_{(S^*/S^-)}$ is the excited state reduction potential, $E_{(S/S^-)}$ is the ground state reduction potential, and $E_g^{\text{opt emis}}$ is the optical energy gap taken as the onset of emission on the high energy side (Figures S7 and S8). The $E_{(S^*/S^-)}$ values for $[Ru^{II}(bpy)_3]^{2+}$ and $Ir(ppy)_3$ vary dramatically by 800−900 mV depending on solvent with $[Ru^{II}(bpy)_3]^{2+}$ being significantly easier to reduce (Table 1, Figure 2). The oxidation potential ($E_{(S^+/S)}$) of the SEDs were measured via CV, and all SEDs used in this study would transfer electrons downhill to a photoexcited $[Ru^{II}(bpy)_3]^{2+}$

DOI: 10.1021/acsaem.8b01560
ACS Appl. Energy Mater. 2019, 2, 37−46

Table 2. Influence of Electron and Proton Sources on the Photocatalytic Reduction of CO_2 with $[Ru^{II}(bpy)_2(CO)_2]^{2+}$ Precatalyst, $[Ru^{II}(bpy)_3]^{2+}$ Photosensitizer and Either MeCN or DMF

						selectivity[a]	
entry	H^+/e^- source	solvent	max CO TOF (h^{-1})	CO (TON)	HCO_2^- (TON)	CO (%)	HCO_2^- (%)
1	BIH	MeCN	57	21	0	100	0
2	BIH/H_2O	MeCN	35	96	177	35	65
3	BIH/TEA	MeCN	91	40	0	100	0
4	BIH	DMF	22	27	0	100	0
5	BIH/H_2O	DMF	62	46	71	39	61
6	BIH/TEA	DMF	42	51	0	100	0
7	BNAH/H_2O	DMF	62	64	80	44	56

[a]Selectivity percentages refer only to the selectivity observed between CO and HCO_2^-. Hydrogen is also observed being only a minor product in most cases (Table S1).

regardless of the solvent choice (Figure S5). However, only BIH was found to produce a downhill electron transfer to photoexcited $Ir^{III}(ppy)_3$. The $E_{(S^+/S)}$ of BNAH is nearly equal to the $E_{(S^*/S^-)}$ of $Ir^{III}(ppy)_3$ indicating electron transfer may be slow from BNAH to $Ir^{III}(ppy)_3$ in DMF. The analogous electron transfer in MeCN could not be analyzed due to insolubility of BNAH in MeCN. Having thermodynamically evaluated each component as potentially suitable for the photocatalytic reduction of CO_2, photocatalysis experiments were conducted.

3.2. Solvent, Proton, and Electron Source Influence. For each variable analyzed (proton and electron sources, photosensitizer, and catalyst), solvent effects on reactivity are analyzed between MeCN and DMF. MeCN and DMF are classic solvents for the photocatalytic reduction of CO_2 with organic solvent soluble molecular catalysts due to CO_2 and charged salt species, such as those formed during electron transfers, having high solubilities. First, electron and proton sources were analyzed by comparing: (1) BIH without an added proton or electron source, (2) BIH with added water as a proton source, (3) BIH with added TEA as a base and potentially an electron source, and (4) BNAH with added water. Anhydrous conditions with BNAH were not analyzed due to the limited solubility of BNAH in the absence of water. BIH has become a popular sacrificial electron donor due in part to a high energy oxidation potential allowing for the use of strongly reducing photosensitizers and the presence of BIH degradation pathways after electron transfer to reduce the number of back electron transfer events. TEA has several potential roles in photocatalytic reactions such as acting (1) as a base which can deprotonate BIH after electron transfer to presumably increase the degradation rate of the BIH cation, (2) as an additional electron source, and (3) as a potential proton source after the TEA cation is generated following an electron transfer. BNAH is a weaker electron donor than BIH, which could slow electron transfers and perhaps favor a particular reaction pathway. Finally, water can play a key role in reactivity with dramatically different rates of reactivity, which are frequently observed in literature.[22,23] Each of these components were systematically analyzed in MeCN and DMF reaction solvents to compare turnover frequency (TOF), TON, and selectivity values.

In MeCN with $[Ru^{II}(bpy)_2(CO)_2]^{2+}$ as precatalyst, $[Ru^{II}(bpy)_3]^{2+}$ as photosensitizer, and only BIH as an added electron source a maximum of 21 turnovers of CO was observed with no formate (Table 2, entry 1; Figure 3). This 100% selectivity toward CO production is possibly due to the absence of a proton source needed to form a metal-hydride intermediate which is often invoked as a key intermediate in catalytic cycles generating formate.[12,24,25] This initial result highlights the control of reaction environment over product selectivity as $[Ru^{II}(bpy)_2(CO)_2]^{2+}$ is reported to primarily make formate.[11] Addition of water to the reaction mixture dramatically changed the product selectivity from 100% CO to 65% favoring formate (Table 2, entry 2; Figure 3). Additionally, the catalyst durability was found to dramatically increase to 273 TONs for carbon reduction products from 21. Interestingly, while the durability of the catalyst significantly increased, the maximum TOF observed for CO production decreased from 57 to 35 h^{-1} (Table 1). This could be due to a slower formate generating catalytic cycle involving a ruthenium-hydride intermediate. Removal of water and the addition of TEA again gave 100% CO product selectivity with a dramatic increase in rate to a TOF of 91 h^{-1} (Table 2, entry 3). The maximum TON doubles relative to anhydrous conditions without TEA (40 versus 21 TON); however, the catalyst still lasts dramatically longer in the presence of water than under anhydrous conditions.

The same set of reaction conditions was evaluated in DMF. Similar TON and selectivity trends were observed in DMF as in MeCN for no additive, added water, and added TEA (Table 2, entries 1−3). TEA was again found in increased durability and rate with 100% CO selectivity relative to without additive, and similar TON values were observed in DMF when compared with MeCN. The maximum TOF values were found to be approximately cut in half for anhydrous conditions regardless of the presence or absence of TEA. Comparing experiments with water added in DMF and MeCN, a significantly lower total TON value was observed in DMF (117 versus 273). However, the maximum observed TOF in DMF was found to be significantly higher than in MeCN (62 versus 35 h^{-1}). Finally, a slightly lower selectivity for formate in the presence of water was observed in DMF (61% versus 65%). These results show reverse reactivities when anhydrous reactions in MeCN and DMF are compared. Anhydrous reactions in MeCN show a higher TOF but lower TON for CO formation than comparable experiments using DMF. But, when water is present, MeCN shows a lower TOF with a higher TON which favors formate production for both solvents. Overall, the product selectivity is weakly influenced by solvent selection with the most dramatic effect being based on the presence or absence of water.

BNAH is a weaker reducing reagent compared to BIH (Table 1). Since BNAH is significantly less soluble in MeCN than BIH, only BNAH in wet DMF was evaluated for comparison with the analogous BIH experiments (Table 2,

DOI: 10.1021/acsaem.8b01560
ACS Appl. Energy Mater. 2019, 2, 37−46

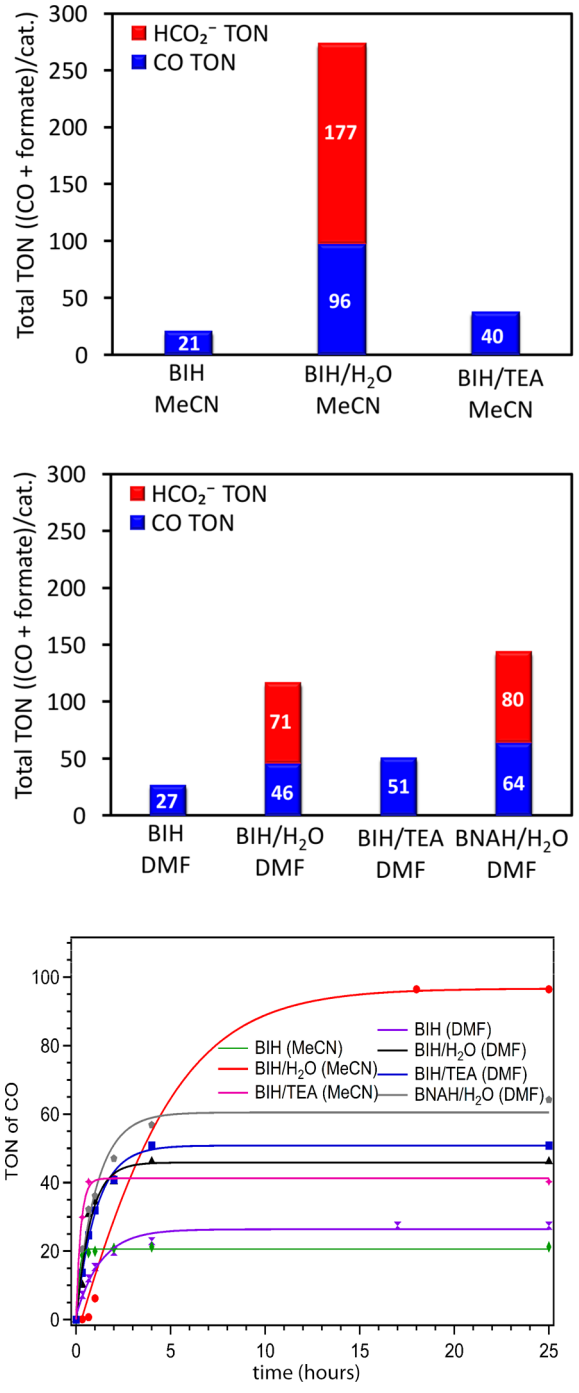

Figure 3. Turnover number graphs showing the influence of electron and proton sources on the photocatalytic reduction of CO_2 with $[Ru^{II}(bpy)_2(CO)_2]^{2+}$ precatalyst, $[Ru^{II}(bpy)_3]^{2+}$ photosensitizer and either MeCN (top) or DMF (middle). CO TON versus time graphs for these same conditions (bottom).

entry 7). The TOF for CO was found to be identical for BNAH and BIH in DMF with water added (62 h^{-1}). A similar durability was noted, with BIH slightly favoring formate selectivity more than BNAH (61% versus 56%). Overall, the replacement of BIH with BNAH was found to have little influence on product selectivity in this case.

3.3. Photosensitizer Influence. Having found that water has a strong influence on product selectivity and catalyst durability, the photosensitizer influence was analyzed in the presence of water (Table 3, Figure 4). Since the use of BIH in wet solvent with $[Ru^{II}(bpy)_2(CO)_2]^{2+}$ as the precatalyst shows a modest selectivity for formate production (65%−61% for the $[Ru^{II}(bpy)_3]^{2+}$ photosensitizer in MeCN and DMF), these conditions were selected for additional analysis with $Ir^{III}(ppy)_3$ as the PS. The low selectivity allows for the observation of potentially more subtle effects from a photosensitizer. $[Ir^{III}(ppy)_3]^-$ is significantly more strongly reducing than $[Ru^{III}(bpy)_3]^{1+}$ and as such offers potentially faster electron transfer kinetics to catalysts according to Marcus theory (−2.6 V versus −1.7 V versus Fc^+/Fc, Table 1).

However, the number of reduced photosensitizer states present in the reaction mixture must also be considered. Emission quenching studies with both photosensitizers were conducted in MeCN with BIH to probe the amount of reduced PS being generated (Figures 5, S10, and S11). The emission intensity of $[Ru^{II}(bpy)_3]^{2+}$ was found to quench dramatically faster than $Ir^{III}(ppy)_3$. For example, a BIH reductant concentration of 50 mM gave a near complete quenching of the $[Ru^{II}(bpy)_3]^{2+}$ emission but only reduced the $Ir^{III}(ppy)_3$ emission intensity by less than half (Figures S10 and S11). A Stern−Volmer plot was generated from these data by plotting the ratio of initial emission intensity (F_0) to final emission intensity (F) at various BIH concentrations (Figure 5). The quenching of both PS emissions was found to be linear in the range of BIH concentrations examined, and the slope of this linear trend gives a Stern−Volmer constant (K_{SV}) of 985 M^{-1} for $[Ru^{II}(bpy)_3]^{2+}$ and 13 M^{-1} for $Ir^{III}(ppy)_3$. The dramatically higher K_{SV} is expected given that the ΔG of electron transfer from BIH to a photoexcited $[Ru^{II}(bpy)_3]^{2+}$ is 630 mV downhill in energy while the analogous ΔG to $Ir^{III}(ppy)_3$ is only 160 mV downhill in energy (Figure 2). Given the higher K_{SV}, the higher molar absorptivity for $[Ru^{II}(bpy)_3]^{2+}$ compared to $Ir^{III}(ppy)_3$ (15,000 versus 11,000 M^{-1} cm^{-1}),[26,27] and broader absorption spectrum (Figure S6), substantially more $[Ru^{II}(bpy)_3]^+$ is expected in the reaction mixture than $[Ir^{III}(ppy)_3]^-$.

A faster electron transfer event could allow for selectivity between reaction pathways leading to CO or formate. Specifically, the formate production pathway likely relies on the formation of a ruthenium-hydride intermediate as a chemical step prior to CO_2 reduction while the CO production pathway relies on a reduction of only the catalyst prior to CO_2 reduction. Electron transfers favoring reduced catalyst formation faster than Ru protonation would then be predicted to favor CO. Indeed, in the presence of $Ir^{III}(ppy)_3$ in MeCN, CO is favored rather than formate which was observed as the major product with $[Ru^{II}(bpy)_3]^{2+}$ as the PS under identical reaction conditions (Table 3, entries 1 and 2; Figure 4). This selectivity was accompanied by a slower maximum TOF (20 versus 35 h^{-1}) and a lower total carbon product TON (Figure 4). These observations can be rationalized as the rate of initial electron transfer either to the catalyst or protonated catalyst controlling product selectivity as being the most uphill of the catalytic cycle which would slow electron transfer from $[Ru^{II}(bpy)_3]^+$ relative to $[Ir^{III}(ppy)_3]^-$. However, the faster TOF of $[Ru^{II}(bpy)_3]^{2+}$ for the generation of CO could be due to a more thermodynamically favorable second electron transfer occurring faster with $[Ru^{II}(bpy)_3]^+$ relative to $[Ir^{III}(ppy)_3]^-$ due to a low concentration of $[Ir^{III}(ppy)_3]^-$. Direct observation and measurement of intermediates within the catalytic cycle are needed to support these hypotheses. We note that $[Ru^{II}(bpy)_3]^{2+}$ has a TON value similar in magnitude

DOI: 10.1021/acsaem.8b01560
ACS Appl. Energy Mater. 2019, 2, 37−46

Table 3. Influence of Photosensitizer on the Photocatalytic Reduction of CO_2 with $[Ru^{II}(bpy)_2(CO)_2]^{2+}$ Catalyst, BIH and H_2O as Proton and Electron Sources, and Either MeCN or DMF

						selectivity[a]	
entry	PS	solvent	max CO TOF (h^{-1})	CO (TON)	HCO_2^- (TON)	CO (%)	HCO_2^- (%)
1	$[Ru^{II}(bpy)_3]^{2+}$	MeCN	35	96	177	35	65
2	$Ir^{III}(ppy)_3$	MeCN	20	100	65	61	39
3	$[Ru^{II}(bpy)_3]^{2+}$	DMF	62	46	71	39	61
4	$Ir^{III}(ppy)_3$	DMF	21	20	0	100	0

[a]Selectivity percentages refer only to the selectivity observed between CO and HCO_2^-. Hydrogen is also observed being only a minor product in most cases (Table S1).

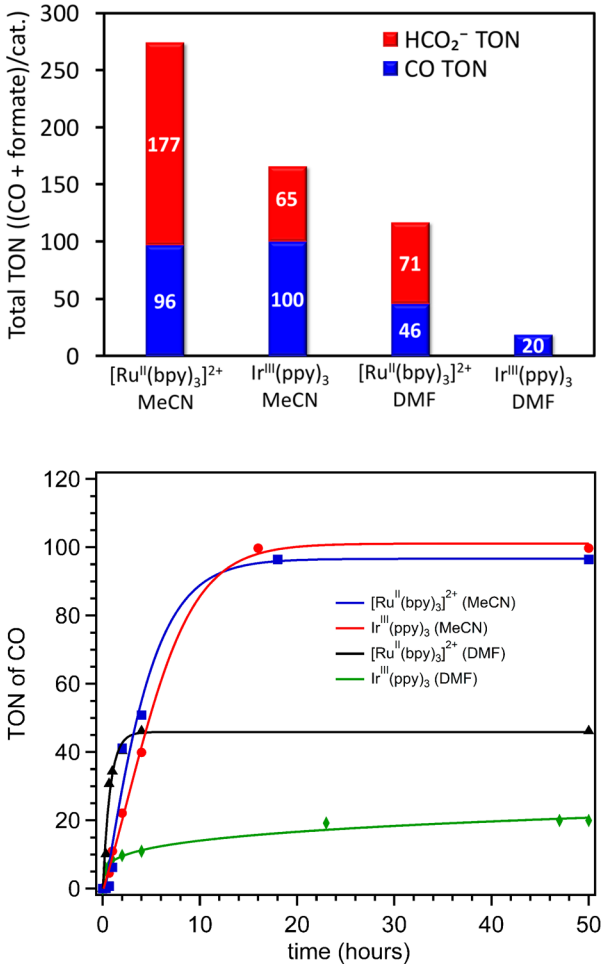

Figure 4. Turnover graph (top) and CO TON versus time graph (bottom) showing the influence of photosensitizer on the photocatalytic reduction of CO_2 with $[Ru^{II}(bpy)_2(CO)_2]^{2+}$ precatalyst, BIH and H_2O as proton and electron sources, and either MeCN or DMF as the solvent.

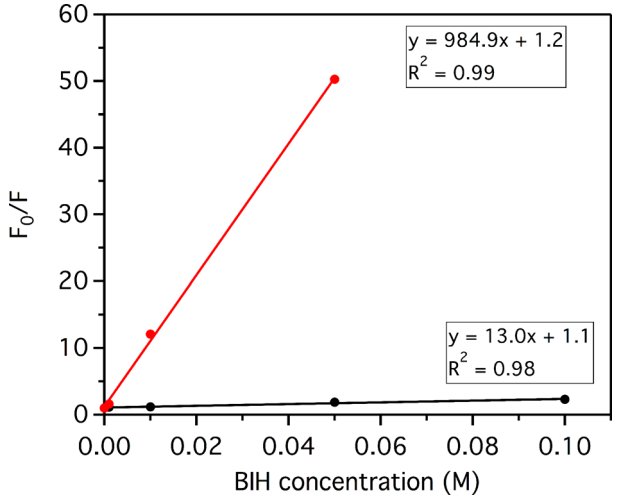

Figure 5. Stern–Volmer quenching plot for $Ir^{III}(ppy)_3$ and $[Ru^{II}(bpy)_3]^{2+}$ in MeCN with varying BIH concentrations.

to that of $Ir^{III}(ppy)_3$ but a faster maximum observed TOF for the former indicates $Ir^{III}(ppy)_3$ PS may be more durable. This agrees with other proposed mechanisms where 2,2′-bipyridyl ligands dissociate more readily than 2-phenylpyridine ligands during photocatalysis.[28]

In DMF, the CO product formation preference with $Ir^{III}(ppy)_3$ was even greater with CO observed as the only product from the reaction (Table 3, entries 3 and 4). The TOF and TON values were notably lower for $Ir^{III}(ppy)_3$ in DMF relative to those for $[Ru^{II}(bpy)_3]^{2+}$. Overall, these results show that the presence of water and $[Ru(bpy)_3]^{2+}$ as a PS favors formate production while anhydrous conditions and $Ir^{III}(ppy)_3$ as a PS favor CO production. Both effects are strong with water being required for formate production, but the selection of solvent and PS allows for 100% selectivity for CO production even in the presence of water.

3.4. Catalyst Influence. Next, the influence of the catalyst on the photocatalytic reduction of CO_2 was analyzed. Conditions which showed the lowest selectivity of the benchmark $[Ru^{II}(bpy)_2(CO)_2]^{2+}$ catalyst and BIH were used to analyze a second ruthenium catalyst since potentially subtle changes in selectivity are most obvious from a poorly selective starting point. $[Ru^{II}(CNC)Cl]^+$ was chosen as the comparison catalyst since a prior report using this catalyst in photoreactions showed a high durability.[10] The energetics of this NHC-ligated catalyst are significantly different with a higher energy reduction potential for $[Ru^{II}(CNC)Cl]^+$ relative to $[Ru^{II}(bpy)_2(CO)_2]^{2+}$ (Table 1, −2.30 V versus −1.32 V in MeCN, respectively). This difference in energetics could play a role in modulating the selectivity of two different reaction pathways if one pathway is more dependent on rapid electron transfers. Additionally, the electron density at the metal center is often higher for NHC-ligated metal complexes which promotes greater nucleophilicity and can lead to reduction of CO_2 to CO after a single electron transfer to the catalyst.[10,23,27,29−33] Given the significant number of differences between the two precatalysts being compared, the ability of a catalyst to control product selectivity under variable environments should be apparent. In MeCN, $[Ru^{II}(CNC)Cl]^+$ was found to be highly selective for CO (97%) in the presence of water with $Ir^{III}(ppy)_3$ as the PS (Table 4, entry 2; Figure 6). Under these identical conditions $[Ru^{II}(bpy)_2(CO)_2]^{2+}$ was

DOI: 10.1021/acsaem.8b01560
ACS Appl. Energy Mater. 2019, 2, 37−46

Table 4. Influence of Catalyst on the Photocatalytic Reduction of CO_2 with a Photosensitizer, BIH and H_2O as Proton and Electron Sources, and Either MeCN or DMF

							selectivity[a]	
entry	catalyst	PS	solvent	max CO TOF (h^{-1})	CO (TON)	HCO_2^- (TON)	CO (%)	HCO_2^- (%)
1	$[Ru^{II}(bpy)_2(CO)_2]^{2+}$	$Ir^{III}(ppy)_3$	MeCN	20	100	65	61	39
2	$[Ru^{II}(CNC)Cl]^+$	$Ir^{III}(ppy)_3$	MeCN	7	227	7	97	3
3	$[Ru^{II}(bpy)_2(CO)_2]^{2+}$	$[Ru^{II}(bpy)_3]^{2+}$	DMF	62	46	71	39	61
4	$[Ru^{II}(CNC)Cl]^+$	$[Ru^{II}(bpy)_3]^{2+}$	DMF	6	16	143	10	90

[a]Selectivity percentages refer only to the selectivity observed between CO and HCO_2^-. Hydrogen is also observed being only a minor product in most cases (Table S1).

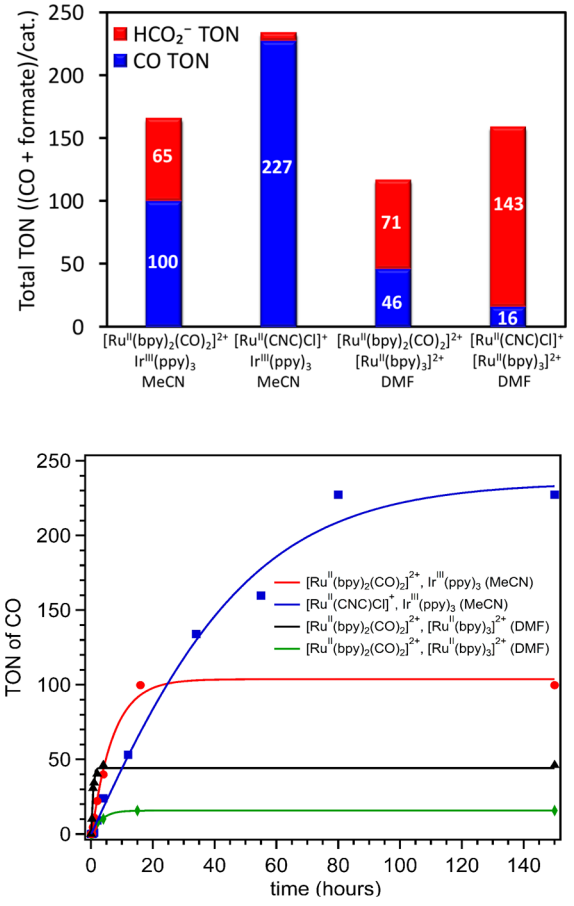

Figure 6. Turnover graph (top) and CO TON versus time graph (bottom) showing the influence of precatalyst on the photocatalytic reduction of CO_2 with a photosensitizer, BIH and H_2O as proton and electron sources, and either MeCN or DMF.

found to be significantly less selective for CO (61%, Table 4, entry 1). The combination of $[Ru^{II}(CNC)Cl]^+$, MeCN, and $Ir^{III}(ppy)_3$ generated the largest selectivity for proton reduction to H_2 as well at 18% H^+ reduction versus CO_2 reduction (Table S1). In contrast, the remainder of the systems studied in this work show either low TON values for proton reduction for systems giving low overall TON values or low percent selectivity for proton reduction in systems giving significant H_2 TON values. The reason for proton reduction increasing significantly for the $[Ru^{II}(CNC)Cl]^+$, MeCN, and $Ir^{III}(ppy)_3$ system is not obvious. Interestingly, in DMF $[Ru^{II}(CNC)Cl]^+$ was found to be significantly more selective for formate production than the $[Ru^{II}(bpy)_2(CO)_2]^{2+}$ with $[Ru^{II}(bpy)_3]^{2+}$ as the PS (90% versus 61%, Table 4, entries 3 and 4). *This suggests that the active catalysts are dramatically influenced by the reaction environment, and a simple classification of a catalyst as favoring CO or formate production irrespective of reaction conditions can be misleading.* In this case, $[Ru^{II}(CNC)Cl]^+$ was found to be more selective for both CO and formate than $[Ru^{II}(bpy)_2(CO)_2]^{2+}$ under different environments.

3.5. Environment Controlled Selectivity. Varying applications may have different environment requirements. Ideally, both a predictable high product selectivity and a high durability are needed for photocatalytic CO_2 reduction reactions. Understanding which reaction components have the strongest influence on product selectivity and catalyst durability is important for rationally designing functional solar fuel systems. One way to probe which components have strong selectivities is through experiments using conditions which have competing selectivities. For example, wet MeCN was found to favor formate production while $Ir^{III}(ppy)_3$ was found to favor CO product. Combining these two variables with the $[Ru^{II}(CNC)Cl]^+$ precatalyst, which seems to accentuate product selectivities, leads to a strong selectivity for CO formation in the presence of water (97% CO selective with a TON of 227; Table 5, entry 1; Figures 7 and S9). Thus, the precatalyst and the PS can be used to select the desired product over the product selectivity imparted from added water. In fact, under conditions which strongly favor CO formation, anhydrous DMF, and $Ir^{III}(ppy)_3$ PS, a similar

Table 5. Highest Selectivities and TON Observed for Each Catalyst under Environments Favoring a Specific Product[a]

								selectivity[b]	
entry	catalyst	solvent	PS	H_2O or TEA	max TOF (h^{-1})	CO (TON)	HCO_2^- (TON)	CO (%)	HCO_2^- (%)
1	$[Ru^{II}(CNC)Cl]^+$	MeCN	$Ir^{III}(ppy)_3$	H_2O	7	227	7	97	3
2	$[Ru^{II}(CNC)Cl]^+$	DMF	$Ir^{III}(ppy)_3$	TEA	9	275	0	100	0
3	$[Ru^{II}(CNC)Cl]^+$	DMF	$[Ru^{II}(bpy)_3]^{2+}$	H_2O	5	16	143	10	90
4	$[Ru^{II}(bpy)_2(CO)_2]^{2+}$	DMF	$Ir^{III}(ppy)_3$	TEA	9	116	0	100	0
5	$[Ru^{II}(bpy)_2(CO)_2]^{2+}$	MeCN	$[Ru^{II}(bpy)_3]^{2+}$	H_2O	35	96	177	35	65

[a]BIH is the electron source in all experiments. [b]Selectivity percentages refer only to the selectivity observed between CO and HCO_2^-. Hydrogen is also observed being only a minor product in most cases (Table S1).

DOI: 10.1021/acsaem.8b01560
ACS Appl. Energy Mater. 2019, 2, 37−46

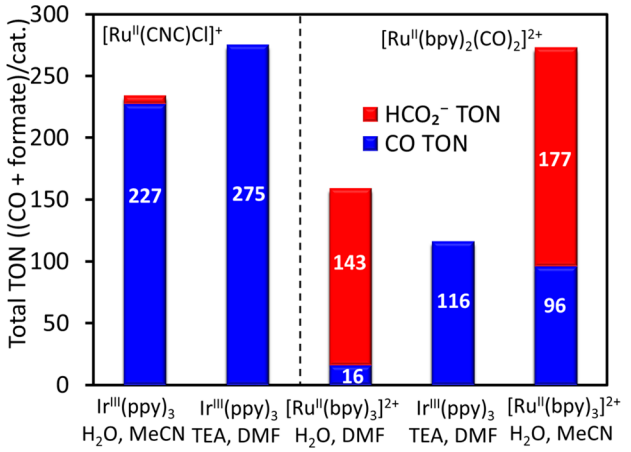

Figure 7. Turnover graphs showing how a combination of environmental parameters can be used to drive the selectivity of either precatalyst.

selectivity and TON value are observed: 100% CO selective and TON of 275 (Table 5, entry 2). However, by changing to wet conditions and changing to a photosensitizer known to favor formate ($[Ru^{II}(bpy)_3]^{2+}$), a dramatically different selectivity is observed for the same catalyst (90% formate, 143 TON for formate; Table 5, entry 3). Similar observations are made with $[Ru^{II}(bpy)_2(CO)_2]^{2+}$ where the PS choice and the presence of water control product selectivities (Table 5, entries 4 and 5). This highlights the critical role the PS is playing in these systems in guiding product selectivity providing water is present.

3.6. Mechanistic Implications. Two plausible catalytic cycles are presented below for CO and formate production based on experimental observations (Scheme 1). Both cycles begin with a precatalyst, $[Ru^{II}(CNC)(MeCN)_2Cl]^+[^-OTf]$. Cyclic voltammetry measurements reveal no significant change in the first reduction potential onset when argon and CO_2 atmospheres are compared, which suggests an electron transfer step happens before a chemical step (e.g., CO_2 complexation or Cl^- dissociation). This suggests the cationic complex is first reduced to a 19-electron neutral complex followed by Cl^- dissociation to open a coordination site.[34] CV measurements also show catalytic activity via a current enhancement under CO_2 compared to argon at the first reduction wave. This suggests that Cl^- dissociation is facile (at least on the CV time scale), and a chemical reaction step happens readily after a coordination site is opened to give the active catalyst **1** (or **A**). This chemical transformation step could be either complexation with CO_2 to give **2** or complexation with a proton to give **B**, which differentiates the mechanistic pathways. We do note there is a second possible, less commonly invoked, cycle to reach formate beginning with metal−carbon bond formation and the eventual protonation of this bond, but we have focused our analysis on the most common pathways to formate which involve M−H bonds.[35,36] Presumably, if this step were irreversible, the catalyst and solvent would play the largest effects in controlling product selectivity. However, the PS was found to have a substantial influence on product selectivity. Within the catalytic cycle, the PS is projected to first have a role after the active catalyst **1** has complexed to CO_2 or a proton. This suggests that the CO_2 complexation step is reversible since the PS results in a product selectivity change. Changing the PS will change the electron transfer rates with strong reducing $Ir^{III}(ppy)_3^-$ presumably having a faster electron transfer event to the catalyst than $[Ru^{II}(bpy)_3]^+$ if Marcus theory kinetics are followed. A reduced rate of reduction of the CO_2 complexed intermediate **2** would allow for an equilibrium to occur between CO_2 binding to the catalyst and the free catalyst which could be protonated potentially leading to a more easily reduced dicationic ruthenium hydride intermediate **B**. It is plausible **B** is slow to form due to low concentration of free protons in the reaction mixture. This is consistent with the stronger reducing $[Ir^{III}(ppy)_3]^-$ being selective for CO formation since **2** can undergo a facile electron transfer based on thermodynamic considerations and may not have time to undergo equilibration. This is a plausible explanation for the critical role the PS is playing in controlling product selectivity. The remaining catalytic cycle steps are postulated as follows.

For the completion of the CO production cycle, intermediate **3** may then add to another CO_2 molecule to generate intermediate **4**. Complex **4** can then be reduced and lose CO_3^{2-} to give the CO complex **6**. Through C-13 labeling studies with $^{13}CO_2$, we observe CO_3^{2-} to be formed by ^{13}C

Scheme 1. Proposed Mechanism for CO Production under Anhydrous Conditions (Left) and Formate Production under Hydrous Conditions (Right)

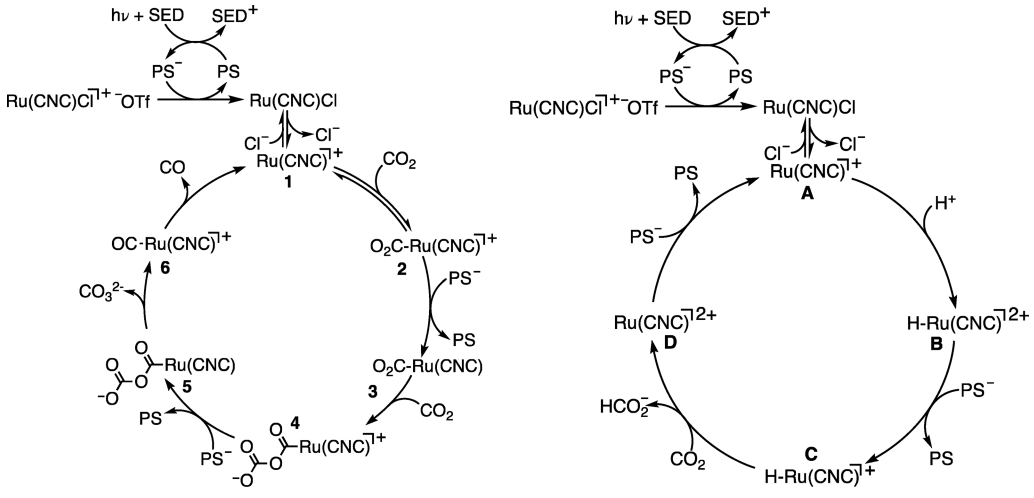

DOI: 10.1021/acsaem.8b01560
ACS Appl. Energy Mater. 2019, 2, 37−46

NMR (Figures S12 and S13). The higher concentration of $[Ru^{II}(bpy)_3]^+$ in the reaction could increase the rate at which **4** is reduced leading to a faster catalytic cycle for $[Ru^{II}(bpy)_3]^{2+}$ despite a slower electron transfer event to **2** relative to $Ir^{III}(ppy)_3$. Catalytic intermediate **6** then can dissociate a CO to free a coordination site and regenerate the active catalyst **1**. Importantly, a second pathway to CO production where protons are added to the reduced CO_2 complex **3** to eventually lead to water as a byproduct instead of a second CO_2 molecule leading to the formation of CO_3^{2-} as a byproduct is possible. This second pathway likely complicates analyzing the relative rates for CO generating photocatalytic reactions evaluated above when comparing wet and anhydrous conditions.

For the completion of the HCO_2^- production cycle, the reduction of dicationic complex **B** generates the monocationic ruthenium hydride complex **C**, which can react with CO_2 to generate formate and dicationic complex **D**. We note that there are two common pathways by which this can occur either via a single step hydride abstraction[37] or via a multiple step CO_2 insertion/M−O bond dissociation mechanism.[25] Either route is plausible given the data currently available. Reduction of complex **D** can then regenerate an initial complex **A**. However, more chemical and computational experiments are needed to further test these hypothesized catalytic cycles as chemical and electron transfer steps could be reversed.

4. CONCLUSIONS

The presence or absence of a proton source and the identity of the photosensitizer was shown to critically influence the selectivity of photocatalytic CO_2 reduction. In contrast, the identity of the solvent, the sacrificial electron donors, and the catalyst structure played a minor supporting role with only a slight influence on selectivity, although significant durability and rate differences were present based on the solvent choice. Water was found to have a dramatic effect on product selectivity and was found to be necessary for formate production. The catalyst structure was found to have some control over product selectivity, but this could be overridden by the choice of photosensitizer when water is present. These results were used to generate a plausible catalytic cycle where a key step (substrate complexation) may be reversible which allows for a rational explanation of how the PS can strongly control product selectivity. Most importantly, this work illustrates that reaction environment is a dominant effect in understanding product selectivity which cannot be ascribed to molecular catalyst design without careful comparisons and control experiments.

■ ASSOCIATED CONTENT

Supporting Information

The Supporting Information is available free of charge on the ACS Publications website at DOI: 10.1021/acsaem.8b01560.

Cyclic voltammograms; emission spectra; UV−vis absorption spectrum; CO TON versus time plot (PDF)

■ AUTHOR INFORMATION

Corresponding Authors

*(J.H.D.) E-mail: delcamp@olemiss.edu.
*(E.T.P.) E-mail: etpapish@ua.edu.

ORCID

Roberta R. Rodrigues: 0000-0003-2930-2451
Chance M. Boudreaux: 0000-0003-1322-9878
Elizabeth T. Papish: 0000-0002-7937-8019
Jared H. Delcamp: 0000-0001-5313-4078

Notes

The authors declare no competing financial interest.

■ ACKNOWLEDGMENTS

We thank NSF (Awards CAT-1800281 and 1800214) for funding this research. Preliminary data were also obtained with NSF OIA-1539035 support.

■ REFERENCES

(1) Robert, M. Running the Clock: CO_2 Catalysis in the Age of Anthropocene. *ACS Energy Lett.* **2016**, *1*, 281−282.
(2) Liu, X.; Inagaki, S.; Gong, J. Heterogeneous Molecular Systems for Photocatalytic CO_2 Reduction with Water Oxidation. *Angew. Chem., Int. Ed.* **2016**, *55*, 14924−14950.
(3) Takeda, H.; Cometto, C.; Ishitani, O.; Robert, M. Electrons, Photons, Protons and Earth-Abundant Metal Complexes for Molecular Catalysis of CO_2 Reduction. *ACS Catal.* **2017**, *7*, 70−88.
(4) Wang, W. H.; Himeda, Y.; Muckerman, J. T.; Manbeck, G. F.; Fujita, E. CO_2 Hydrogenation to Formate and Methanol as an Alternative to Photo- and Electrochemical CO_2 Reduction. *Chem. Rev.* **2015**, *115*, 12936−12973.
(5) Benson, E. E.; Kubiak, C. P.; Sathrum, A. J.; Smieja, J. M. Electrocatalytic and Homogeneous Approaches to Conversion of CO_2 to Liquid Fuels. *Chem. Soc. Rev.* **2009**, *38*, 89−99.
(6) Aresta, M.; Dibenedetto, A.; Angelini, A. Catalysis for the Valorization of Exhaust Carbon: From CO_2 to Chemicals, Materials, and Fuels. Technological Use of CO_2. *Chem. Rev.* **2014**, *114*, 1709−1742.
(7) Morris, A. J.; Meyer, G. J.; Fujita, E. Molecular Approaches to the Photocatalytic Reduction of Carbon Dioxide for Solar Fuels. *Acc. Chem. Res.* **2009**, *42*, 1983−1994.
(8) Hammer, N. I.; Sutton, S.; Delcamp, J. H.; Graham, J. D. Photocatalytic Water Splitting and Carbon Dioxide Reduction. *Handbook of Climate Change Mitigation and Adaptation*; Springer: Cham, Switzerland, 2016; pp 2709−2756, DOI: 10.1007/978-3-319-14409-2_46.
(9) Sahara, G.; Ishitani, O. Efficient Photocatalysts for CO_2 Reduction. *Inorg. Chem.* **2015**, *54*, 5096−5104.
(10) Boudreaux, C. M.; Liyanage, N. P.; Shirley, H.; Siek, S.; Gerlach, D. L.; Qu, F.; Delcamp, J. H.; Papish, E. T. Ruthenium(II) Complexes of Pyridinol and N-Heterocyclic Carbene Derived Pincers as Robust Catalysts for Selective Carbon Dioxide Reduction. *Chem. Commun.* **2017**, *53*, 11217−11220.
(11) Ishida, H.; Terada, T.; Tanaka, K.; Tanaka, T. Photochemical CO_2 Reduction Catalyzed by $[Ru(bpy)_2(CO)_2]^{2+}$ Using Triethanolamine and 1-Benzyl-1,4-Dihydronicotinamide as an Electron Source. *Inorg. Chem.* **1990**, *29*, 905−911.
(12) Fei, H.; Sampson, M. D.; Lee, Y.; Kubiak, C. P.; Cohen, S. M. Photocatalytic CO_2 Reduction to Formate Using a Mn(I) Molecular Catalyst in a Robust Metal-Organic Framework. *Inorg. Chem.* **2015**, *54*, 6821−6828.
(13) Heldebrant, D. J.; Jessop, P. G.; Thomas, C. A.; Eckert, C. A.; Liotta, C. L. The Reaction of 1,8-Diazabicyclo[5.4.0]undec-7-ene (DBU) with Carbon Dioxide. *J. Org. Chem.* **2005**, *70*, 5335−5338.
(14) Rillema, D. P.; Allen, G.; Meyer, T. J.; Conrad, D. Redox Properties of Ruthenium(II) Tris Chelate Complexes Containing the Ligands 2,2'-Bipyrazine, 2,2'-Bipyridine, and 2,2'-Bipyrimidine. *Inorg. Chem.* **1983**, *22*, 1617−1622.
(15) Ohsawa, Y.; Sprouse, S.; King, K. A.; DeArmond, M. K.; Hanck, K. W.; Watts, R. J. Electrochemistry and Spectroscopy of Ortho-Metalated Complexes of Ir(III) and Rh(III). *J. Phys. Chem.* **1987**, *91*, 1047−1054.
(16) Marcus, R. A. Chemical and Electrochemical Electron-Transfer Theory. *Annu. Rev. Phys. Chem.* **1964**, *15*, 155−196.

DOI: 10.1021/acsaem.8b01560
ACS Appl. Energy Mater. 2019, 2, 37−46

(17) Marcus, R. A. On the Theory of Oxidation-Reduction Reactions Involving Electron Transfer. I. *J. Chem. Phys.* **1956**, *24*, 966−978.
(18) Silverstein, T. P. Marcus Theory: Thermodynamics Can Control the Kinetics of Electron Transfer Reactions. *J. Chem. Educ.* **2012**, *89*, 1159−1167.
(19) Pegis, M. L.; Roberts, J. A.; Wasylenko, D. J.; Mader, E. A.; Appel, A. M.; Mayer, J. M. Standard Reduction Potentials for Oxygen and Carbon Dioxide Couples in Acetonitrile and *N,N*-Dimethylformamide. *Inorg. Chem.* **2015**, *54*, 11883−11888.
(20) Kolthoff, I. M.; Chantooni, M. K.; Smagowski, H. Acid-Base Strength in *N,N*-Dimethylformamide. *Anal. Chem.* **1970**, *42*, 1622−1628.
(21) Costentin, C.; Drouet, S.; Robert, M.; Saveant, J. M. A Local Proton Source Enhances CO_2 Electroreduction to CO by a Molecular Fe Catalyst. *Science* **2012**, *338*, 90−94.
(22) Carpenter, C. A.; Brogdon, P.; McNamara, L. E.; Tschumper, G. S.; Hammer, N. I.; Delcamp, J. H. A Robust Pyridyl-NHC-Ligated Rhenium Photocatalyst for CO_2 Reduction in the Presence of Water and Oxygen. *Inorganics* **2018**, *6*, 22.
(23) Liyanage, N. P.; Dulaney, H. A.; Huckaba, A. J.; Jurss, J. W.; Delcamp, J. H. Electrocatalytic Reduction of CO_2 to CO with Re-Pyridyl-NHCs: Proton Source Influence on Rates and Product Selectivities. *Inorg. Chem.* **2016**, *55*, 6085−6094.
(24) Taheri, A.; Thompson, E. J.; Fettinger, J. C.; Berben, L. A. An Iron Electrocatalyst for Selective Reduction of CO_2 to Formate in Water: Including Thermochemical Insights. *ACS Catal.* **2015**, *5*, 7140−7151.
(25) Agarwal, J.; Johnson, R. P.; Li, G. Reduction of CO_2 on a Tricarbonyl Rhenium(I) Complex: Modeling a Catalytic Cycle. *J. Phys. Chem. A* **2011**, *115*, 2877−2881.
(26) Yoshimura, A.; Hoffman, M. Z.; Sun, H. An Evaluation of the Excited State Absorption Spectrum of $Ru(bpy)_3^{2+}$ in Aqueous and Acetonitrile Solutions. *J. Photochem. Photobiol., A* **1993**, *70*, 29−33.
(27) Huckaba, A. J.; Sharpe, E. A.; Delcamp, J. H. Photocatalytic Reduction of CO_2 with Re-Pyridyl-NHCs. *Inorg. Chem.* **2016**, *55*, 682−690.
(28) Rao, H.; Bonin, J.; Robert, M. Toward Visible-Light Photochemical C CO_2-to-CH_4 Conversion in Aqueous Solutions Using Sensitized Molecular Catalysis. *J. Phys. Chem. C* **2018**, *122*, 13834−13839.
(29) Burks, D. B.; Davis, S.; Lamb, R. W.; Liu, X.; Rodrigues, R. R.; Liyanage, N. P.; Sun, Y.; Webster, C. E.; Delcamp, J. H.; Papish, E. T. Nickel(II) Pincer Complexes Demonstrate That the Remote Substituent Controls Catalytic Carbon Dioxide Reduction. *Chem. Commun.* **2018**, *54*, 3819−3822.
(30) Cope, J. D.; Liyanage, N. P.; Kelley, P. J.; Denny, J. A.; Valente, E. J.; Webster, C. E.; Delcamp, J. H.; Hollis, T. K. Electrocatalytic Reduction of CO_2 with CCC-NHC Pincer Nickel Complexes. *Chem. Commun.* **2017**, *53*, 9442−9445.
(31) Stanton, C. J., 3rd; Vandezande, J. E.; Majetich, G. F.; Schaefer, H. F., 3rd; Agarwal, J. Mn-NHC Electrocatalysts: Increasing π Acidity Lowers the Reduction Potential and Increases the Turnover Frequency for CO_2 Reduction. *Inorg. Chem.* **2016**, *55*, 9509−9512.
(32) Stanton, C. J., 3rd; Machan, C. W.; Vandezande, J. E.; Jin, T.; Majetich, G. F.; Schaefer, H. F., 3rd; Kubiak, C. P.; Li, G.; Agarwal, J. Re(I) NHC Complexes for Electrocatalytic Conversion of CO_2. *Inorg. Chem.* **2016**, *55*, 3136−3144.
(33) Agarwal, J.; Shaw, T. W.; Stanton, C. J., III; Majetich, G. F.; Bocarsly, A. B.; Schaefer, H. F., III. NHC-Containing Manganese(I) Electrocatalysts for the Two-Electron Reduction of CO_2. *Angew. Chem., Int. Ed.* **2014**, *53*, 5152−5155.
(34) Machan, C. W.; Sampson, M. D.; Chabolla, S. A.; Dang, T.; Kubiak, C. P. Developing a Mechanistic Understanding of Molecular Electrocatalysts for CO_2 Reduction Using Infrared Spectroelectrochemistry. *Organometallics* **2014**, *33*, 4550−4559.
(35) Francke, R.; Schille, B.; Roemelt, M. Homogeneously Catalyzed Electroreduction of Carbon Dioxide-Methods, Mechanisms, and Catalysts. *Chem. Rev.* **2018**, *118*, 4631−4701.
(36) Ishida, H.; Tanaka, K.; Tanaka, T. Electrochemical CO_2 Reduction Catalyzed by $[Ru(bpy)_2(CO)_2]^{2+}$ and $[Ru(bpy)_2(CO)Cl]^+$. The Effect of Ph on the Formation of CO and HCOO-. *Organometallics* **1987**, *6*, 181−186.
(37) Johnson, S. I.; Nielsen, R. J.; Goddard, W. A. Selectivity for HCO_2^- over H_2 in the Electrochemical Catalytic Reduction of CO_2 by (POCOP)IrH_2. *ACS Catal.* **2016**, *6*, 6362−6371.

DOI: 10.1021/acsaem.8b01560
ACS Appl. Energy Mater. 2019, 2, 37−46